

Function and Electronic Structure of the SnO_2 Buffer Layer between the $\alpha\text{-Fe}_2\text{O}_3$ Water Oxidation Photoelectrode and the Transparent Conducting Oxide Current Collector

Published as part of *The Journal of Physical Chemistry virtual special issue "D. D. Sarma Festschrift"*.

Yelin Hu, Florent Boudoire, Matthew T. Mayer, Songhak Yoon, Michael Graetzel, and Artur Braun*

Cite This: *J. Phys. Chem. C* 2021, 125, 9158–9168

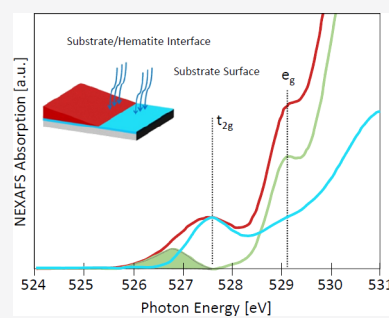
Read Online

ACCESS |

Metrics & More

Article Recommendations

ABSTRACT: The tin oxide buffer layer between the transparent conducting oxide current collector and the hematite photoelectrode causes considerable water oxidation enhancement of that electrode. The water oxidation onset potential is lowered by 180 mV. The lifetime of photogenerated charge carriers is increased by a factor of 10. For the investigation of structure and function of the buffer layer, we designed a wedge-shaped multilayer film assembly. Oxygen 1s X-ray photoemission spectra suggest a decrease of oxygen vacancy concentration near the interface of $\alpha\text{-Fe}_2\text{O}_3$ and FTO– SnO_2 , when the SnO_2 buffer layer is introduced. This SnO_2 buffer layer increases the crystallinity of the hematite layer. The oxygen 1s near-edge X-ray absorption fine structure shows that the buffer layer increases the Fe 3d–O 2p hybridization and affects the quasi-Fermi level of electrons in $\alpha\text{-Fe}_2\text{O}_3$. There is some indication that the $\alpha\text{-Fe}_2\text{O}_3$ layer contains an adverse hole state in the valence band which disappears when the $\alpha\text{-Fe}_2\text{O}_3$ layer is grown on the SnO_2 layer. This layer induces improved orbital overlap with subsequent improved charge transfer between the absorber $\alpha\text{-Fe}_2\text{O}_3$ and the current collector FTO. Our experiments indicate that performance enhancement by this buffer layer is of electronic structure origin.



INTRODUCTION

Hematite ($\alpha\text{-Fe}_2\text{O}_3$) is an extensively studied photoanode material for solar water splitting in single junction electrode design. This material is of interest because of its abundance, stability, and its suitable band gap with valence band edge position as well as its potential for high quantum conversion efficiency. The performance of the hematite electrode is limited by the short hole diffusion length (2–4 nm)¹ as compared to the long light penetration depth ($\alpha^{-1} = 118$ nm at $\lambda = 550$ nm).² Only those photogenerated holes, which are in proximity to the semiconductor–liquid junction (SCLJ), would pass the space charge layer and contribute to water oxidation, whereas most holes created in the bulk would recombine with electrons before reaching the surface. Therefore, for efficient water splitting on hematite, the charge separation and charge transfer process of photogenerated holes at the semiconductor–liquid junction must be addressed. This disaccord can be circumvented by the development of nanostructured films with a few nanometer thickness, and thus the photogenerated holes can reach the SCLJ before recombination.³ Promising approaches are highly structured host scaffold–guest absorber architectures^{4–7} or semiconductor nanostructures.^{8,9}

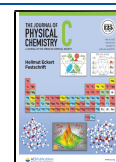
Ultrathin hematite films deposited by spray pyrolysis,^{10–15} atomic layer deposition,^{16–19} sol–gel process,^{20,21} and other

methods, however, exhibit low photoactivity on many substrates (Au, Pt, fluorine-doped tin oxide, and WO_3). This “inactivity” of ultrathin hematite films has been attributed to the interaction of $\alpha\text{-Fe}_2\text{O}_3$ with fluorine-doped tin oxide (FTO)^{22,23} during operation. This interaction widens the Fe 3d–O 2p hybridized states and in return decreases the degree of p–d orbital hybridization. This effect enhances the recombination of photogenerated holes and electrons. It has been shown^{14,24,25} that the photoelectrochemical losses are related to the relatively low degree of crystallinity of deposited $\alpha\text{-Fe}_2\text{O}_3$ on FTO, which was found to correlate with absorbance and photocatalytic water oxidation performance. This hampers further successful implementation of the host–guest approach for efficient utilization of hematite.^{4,5,26,27} Previous studies with the atmospheric pressure chemical vapor deposition (APCVD) of Fe_2O_3 suggested the beneficial effect of a pretreatment of tetraethyl orthosilicate (TEOS).²⁸ This finding suggests that interfacial layers²⁹ between absorber and

Received: February 28, 2021

Revised: April 1, 2021

Published: April 26, 2021



current collector may play a decisive role in the transport properties of the electrode assembly and that the integration of a buffer layer³⁰ is a promising device engineering avenue for the performance improvement of photoelectrodes. The importance of such buffer layers is demonstrated by many examples, such as the enhanced photoactivity of hematite photoanodes deposited on FTO conducting substrate modified with SiO_2 ,¹⁴ TiO_2 ,^{12,31,32} Nb_2O_5 ,¹² and Ga_2O_3 ,^{11,25} as well as SnO_2 ,³³ or Al_2O_3 .³⁴ The underlying mechanisms for the benign function of buffer layer for hematite photoanodes have been under debate.^{12,14,34} It was suggested that besides improving the crystallinity and uniformity of deposited hematite films, the role of these films also lies in an increase in electron doping in the hematite film.

Herein we study the interface between the $\alpha\text{-Fe}_2\text{O}_3$ absorber film and the SnO_2 buffer layer on the FTO current collector. The ultrathin hematite sample with the SnO_2 buffer layer underneath shows dramatic enhancement on photoelectrochemical response. It causes a favorable shift of the onset potential of photocurrent to 1.03 V versus the reversible hydrogen electrode (RHE), accompanied by increased lifetime of charge carriers. Grazing incidence X-ray diffraction (GIXRD) was utilized to investigate crystallinity of ultrathin hematite films with and without employing the SnO_2 buffer layer. We focus on studying the electronic structure of region between $\alpha\text{-Fe}_2\text{O}_3$ and SnO_2 buffer layer by X-ray photoemission spectroscopy (XPS) and near-edge X-ray absorption fine structure (NEXAFS) spectroscopy.

METHODS

Unless otherwise noted, all reagents were used without further purification. Ethanol (98%) was obtained from Aldrich. Conducting fluorine-doped tin oxide (FTO)-coated glass substrates had a sheet resistance of $7\ \Omega/\text{cm}$ and 5% haze, supplied by Solaronix, Switzerland. The FTO layer is 250 nm thick. Prior to use, the FTO glass was subjected to ultrasonic cleaning using deconex surfactant and ethanol and then treated by UV-O_3 . The tin source tetrakis(dimethylamino)tin(IV) (TDMASn, AB111631, ABCR) was used as received.

Buffer Layer Deposition. Tin oxide layers were deposited on the FTO by atomic layer deposition using a Savannah 100 instrument (Cambridge Nanotechnology) in conjunction with an UV-ozone generator (Yanco Industries LTD). TDMASn was pulsed into a nitrogen flow (20 ssm, Carbagas, 99.9999% purity) at $55\ ^\circ\text{C}$. The manifold between the precursors and reactor chamber was maintained at $150\ ^\circ\text{C}$, and the reactor chamber was maintained at $120\ ^\circ\text{C}$. One single SnO_2 deposition cycle is with the following sequence: close, 0.5 s TDMASn, 10 s delay, open, 15 s delay, close, 0.1 s O_3 pulse, 10 s delay, open, 15 s delay. The coating apparatus is calibrated such that 25 single cycles yield a film with 3 nm thickness. One such 3 nm thin SnO_2 buffer layer was deposited with 25 single cycles.

Ultrathin Hematite Deposition. We looked at two different electrode architectures with each 100 nm thick iron oxide films. (1) Iron oxide was directly deposited on the FTO coated glass, and (2) iron oxide was coated on the SnO_2 layer, which was coated on FTO. For the iron oxide deposition we used ultrasonic spray pyrolysis (USP). The surface temperature of the hot plate was $415\ ^\circ\text{C}$. The iron precursor was 10 mM $\text{Fe}(\text{acac})_3$ (99.9%) solution. The feeding speed was 12 mL/min, and total amount of precursor used was 20 mL. Wedge-shaped hematite films with 100 nm thickness at the

thick end for NEXAFS and XPS measurements with gradient thickness were also deposited by using USP.

Grazing Incidence X-ray Diffraction (GIXRD). GIXRD was performed by using a PANalytical X'Pert PRO MPD system equipped with an X-ray mirror and a parallel-beam collimator. The incident X-rays had a wavelength of 1.5418 Å, and the incident angle was fixed to 1° . X-ray diffractograms were recorded from 20° to 80° (2θ) with an angular step interval of 0.017° .

Electrochemical Characterization. Photocurrents were recorded in 1 M NaOH aqueous solution ($\text{pH} = 13.6$) by using a three-electrode configuration photoelectrochemical cell (so-called cappuccino cell), with $\text{Ag}^+/\text{AgCl}/\text{sat. KCl}$ as the reference electrode and a platinum plate ($0.5\ \text{cm} \times 0.5\ \text{cm}$) as the counter electrode. Simulated solar light was generated from a Lot-Oriel solar simulator passing through a KG 3 filter (3 mm, Schott) with a measured intensity equivalent to standard AM 1.5 G sunlight. The illumination area is controlled by a face mask on the three-electrode cell to $0.5\ \text{cm}^2$. The potential was swept anodically from 0.7 to 1.7 V vs RHE at a scan rate of $10\ \text{mV s}^{-1}$ by Ivium Stat (IVIUMSTAT).

Mott–Schottky measurements were performed with the same three-electrode cell in the dark. Impedance spectra were measured at frequencies from 1 MHz to 1 Hz with a sinusoidal potential perturbation by the same potentiostat used in the photoelectrochemical measurement. The bias potential was scanned from 1.5 to 0.7 V vs RHE. The capacitance was extracted from the least-squares fits according to the two-Randle-circle model³⁵ treated with Zview (Scribner Associates).

X-ray Spectroscopy Measurement. Near-edge X-ray absorption fine structure (NEXAFS) and core level XPS spectra were recorded at beamline 9.3.2 of the Advanced Light Source in Lawrence Berkeley National Laboratory, USA. The energy resolution of the beamline was $E/\Delta E = 3000$. The spot size of the beam was $500\ \mu\text{m} \times 1500\ \mu\text{m}$. The base pressure of the main chamber was 10^{-9} Torr during measurements. The XPS spectra were measured by using photon energies of 635 eV for the highest counting number. The X-ray energy axis was calibrated by using $\text{C } 1s = 285\ \text{eV}$.

Kelvin Probe Measurement. Work functions were measured by a single point Kelvin probe (KP020, KP Technology) on samples with gradient thickness of hematite samples. The tip was scanned from the hematite-free area to the hematite-rich area. The substrate/hematite boundary was identified by surface photovoltage response. All measurements were performed in an Ar atmosphere. A gold sheet served as the reference sample.

RESULTS AND DISCUSSION

We begin with the photoelectrochemical characteristic of the SnO_2 buffer layer on hematite photoanodes. Prior to hematite deposition, the FTO conducting substrate was conformal coated with SnO_2 by atomic layer deposition (ALD, ca. 3 nm). We synthesized hematite films through ultrasonic spray pyrolysis from a solution of iron(III) acetylacetonate because of its good film uniformity and good photoelectrode performance.³⁶ Figure 1a shows photocurrent–voltage (J – V) curves of hematite deposited on FTO and FTO– SnO_2 substrates measured in 1 M NaOH electrolyte with simulated solar irradiation of air mass (AM) 1.5. The potential was swept at a low scan rate of 10 mV/s from cathodic to anodic potentials so as to minimize the current from the double-layer

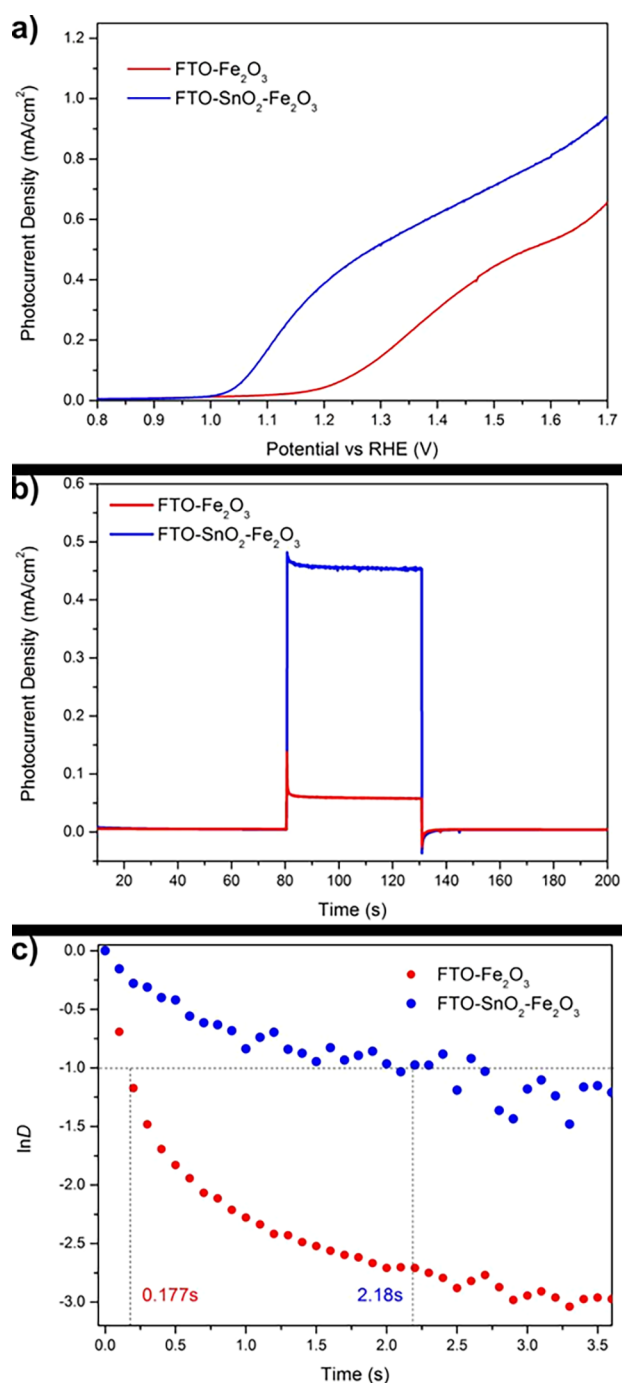


Figure 1. (a) Comparison of the current–voltage characteristics of FTO–Fe₂O₃ and FTO–SnO₂–Fe₂O₃ under simulated sunlight at a scan rate of 10 mV/s. (b) Transient photocurrent dynamics at 1.23 V_{RHE} applied bias. (c) Anodic transient dynamics under at 1.23 V_{RHE} bias.

capacitance.³⁷ Without buffer layer, the electrode exhibits a typical response of an ultrasonic spray pyrolysis (USP) grown ultrathin hematite sample (red line, FTO–Fe₂O₃), with the water oxidation photocurrent onset potential as high as +1.21 V vs the reversible hydrogen electrode (RHE) reference. The photocurrent density reaches 0.06 and 0.35 mA/cm² at 1.23 and 1.43 V bias vs RHE, respectively. Adding the 3 nm SnO₂ buffer layer onto the FTO substrate dramatically improves the performance of the ultrathin hematite film (blue line, FTO–SnO₂–Fe₂O₃). With the SnO₂ layer underneath, the photo-

current onset is beneficially shifted to cathodic direction by approximately 0.18–1.03 V vs RHE. The current density reaches 0.45 and 0.65 mA/cm² at 1.23 and 1.43 V vs RHE bias, respectively. The photocurrent density of this assembly is superior to that of the control FTO–Fe₂O₃ sample over the entire bias potential range.

From the *J/V* characteristics, we find an ~180 mV cathodic shift of the photocurrent onset when a SnO₂ buffer layer is applied. The shift of the onset potential is a manifestation of the competition between water oxidation and a charge carrier recombination process at the SCLJ. The characteristic transient photocurrent was therefore studied to investigate the effect of SnO₂ buffer layer as shown in Figure 1b. The current densities were obtained at a bias of 1.23 V vs RHE. When the solar simulator light is switched on, an anodic current spike is observed, arising from accumulation of photogenerated holes either at the photoanode surface or from the “oxidation” of trap states.

The initial current density (*I*_{in}) of the FTO–Fe₂O₃ sample is 0.14 mA/cm², which rapidly decreases to a steady state current density (*I*_{st}) around 0.06 mA/cm², due to the perturbation of accumulated holes on the charge distribution in the space charge layer. The *I*_{in} of the FTO–SnO₂–Fe₂O₃ electrode assembly is 0.48 mA/cm² and decreases to 0.45 mA/cm² for *I*_{st}, indicating a diminished current density loss from charge recombination after applying the SnO₂ buffer layer. Our observation indicates that in the presence of the buffer layer photoexcited holes could escape easily from trap states on the photoanode surface or at the substrate/hematite interface. To quantitatively determine the charge recombination behavior, we define a parameter (*D*) so as to normalize the photocurrent transient behavior in Figure 1c.³⁸

$$D = \frac{I(t) - I(st)}{I(in) - I(st)}$$

where *I*(*in*) is the current density at time as shown in Figure 1b. The time when ln *D* = −1 in the normalized plots of ln *D*–*t* (Figure 1c) is defined as the transient time constant (*τ*), reflecting the charge carrier dynamics, i.e., charge recombination and lifetime of the charge carriers. The time constant *τ* was estimated to 2.18 s for the FTO–SnO₂–Fe₂O₃ electrode, which is around 12 times of *τ* for the FTO–Fe₂O₃ sample (~0.18 s), underpinning the suppressed charge recombination due to the presence of the SnO₂ buffer layer. In addition to water oxidation kinetics, the transient behavior is also influenced by the crystallinity of the deposited hematite.^{14,39–41}

Because of the small thickness of the films, a rigorous crystallographic analysis would be very challenging and beyond the scope of this work. For crystallographic analysis, we performed grazing incidence X-ray diffraction (GIXRD) as shown in Figure 2. Two principal Bragg reflections are observed centered at 38° and 51.83° (2*θ*) for all diffractograms, corresponding to the (200) and (211) planes of the FTO layer according to the SnO₂ diffraction patterns from reference JCPDS No. 77-0452. Because the GIXRD patterns of both samples are virtually identical, it appears that the crystal structure of FTO–SnO₂ (green line) and FTO (black line) are indistinguishable. This is reasonable because we do not expect a 3 nm thin film synthesized at 120 °C to produce a diffraction pattern with peaks. There are two peaks due to α-Fe₂O₃ (hematite), namely the (104) and (110) reflection in

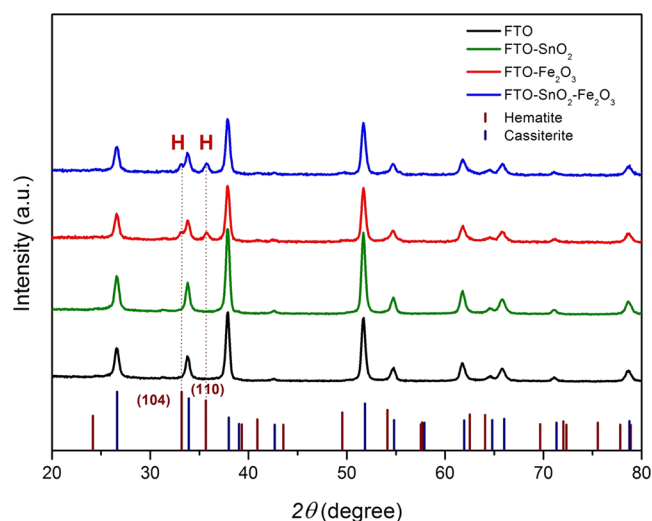


Figure 2. Grazing incidence X-ray diffraction patterns of FTO glass (black), FTO-SnO₂ (olive), FTO-Fe₂O₃ (red), and FTO-SnO₂-Fe₂O₃ (blue) films.

hexagonal coordinates, respectively, on both diffractograms of FTO-Fe₂O₃ (red line) and FTO-SnO₂-Fe₂O₃ (blue line) films. We cannot make out any other phases than hematite because of the relatively low diffraction intensity from ultrathin hematite film (10–18 nm¹⁴). The stronger (110) reflection peak indicates that the deposited hematite film has a (110) texture. Because hematite has a highly anisotropic electron transport along the iron bilayer (110) basal plane, a (110) dominant feature would be indicative to enhanced charge transport and reduced electron–hole recombination. We chose the (110) plane for the determination of the crystallite size of the ultrathin hematite films using the Scherrer equation. The intensity of the (110) peak is large enough to be interpreted as the result of a texture and also large enough for quantitative analysis with Scherrer's formula. The average crystallite size d is determined as³⁸

$$d = \frac{K\lambda}{\beta \cos \theta}$$

where K is a shape factor, λ is the wavelength of incident X-ray beam, β is the broadening of the diffraction line measured in radians at half of its maximum intensity (FWHM), θ is Bragg's angle, and d is the diameter of the crystallite. The average crystallite size of the hematite film on the FTO substrate (from GIXRD data) was found to be 27.7 nm. Upon insertion of the SnO₂ buffer layer, the crystallite size increases by around 50% to 42.2 nm. Given this large increase, it was not necessary to take into account the instrument broadening. The outcome is consistent with comparable studies where crystal growth was observed. Increased crystallite size was observed both for hematite films annealed over 600 °C^{20,42} and for ultrathin electrodes with multiple metal oxide layers (including Nb₂O₅, SiO₂, and Ga₂O₃),^{14,25} which all exhibit improved photoelectrochemical performance.

The diffraction data therefore confirm that the SnO₂ layer acts like a buffer layer, which improves the crystallinity of the hematite film. Hisatomi et al.^{11,12} suggested that an underlayer could serve as isomorphic template for growth of ultrathin hematite films. It might also act as a lattice strain buffer with which iron oxide is distanced from the strain and disorder from substrate/film interface.^{11,14} While we see no evidence for that

it is a plausible scenario, Pailhé²⁴ suggests that the control of the crystallite size of hematite could tune the trigonal distortion of the Fe³⁺ octahedral sites, which directly influences the crystal field intensity and the energy positions of the charge transfer bands and d–d absorption bands in the visible–NIR range. This results in a stronger light absorbance. We do not believe, however, that this effect extends over the entire thickness of the hematite film, which at maximum is 100 nm. In addition, increased particle size directly enables the structural relaxation. Such correlation between the structural relaxation effect and photoactivity was observed for mesoporous hematite films annealed at various temperatures.⁴² The enhanced crystalline quality of the hematite film mediated by the SnO₂ buffer layer goes along with a lower density of defects as trapping states. The hole mobility would thus be improved, leading to a higher charge collection efficiency near the substrate/hematite interface and/or on the hematite surface.

The diffraction analysis points to the crystallographic structure origin of the drastic change in the photoelectrochemical property of the FTO-SnO₂-Fe₂O₃ electrode. The buffer layer, however, also affects the electronic structure of the interface region between hematite and substrate as less interfacial recombination from improved long-range order.

Itoh²² suggested that for ultrathin hematite on the bare FTO conducting substrate the electron cloud of FTO extends into the iron oxide absorber film, thus causing enhanced electron–hole recombination and diminished photoactivity. Such negative interfacial interaction was observed on various substrates, Au, Pt, and WO₃, for instance.¹⁴ A similar conclusion was made by other researchers,^{20,42} and it was suggested that by the high-temperature annealing of the hematite such recombination could be diminished. The NEXAFS spectra recorded from the FTO/ α -Fe₂O₃ interface show that the interface is associated with a distribution of unoccupied oxygen p-hybridized states located below the lowest unoccupied conduction band, which emerge from the displacement of Fe³⁺ ions in the corundum structure.²³ High-temperature processing could diminish these states and improve the degree of p–d orbital hybridization of hematite films as well. The back-injection of electrons from FTO to α -Fe₂O₃ can be suppressed by the interaction of α -Fe₂O₃ with the buffer layer.¹² The possibility of such interaction of α -Fe₂O₃ with the SnO₂ buffer layer is supported by the band bending of hematite at the substrate/hematite interface, which we have determined from the changes ϕ of the work function via the Kelvin probe, taking the clean gold surface with work function $\Phi_{\text{Au}} = 5.1$ eV as reference. The work function change measured over the photoelectrode surface is 0.79 eV for the simple FTO-Fe₂O₃ electrode (FF), but with the engineering of the SnO₂ buffer layer (FSF) the work function change increases to $\phi = 0.92$ eV. The work functions are thus $\Phi_{\text{FF}} = 4.31$ eV and $\Phi_{\text{FSF}} = 4.18$ eV. This change of 130 meV is in the same order of the cathodic shift of water splitting onset potential (180 meV). A stronger band bending in the interface region of the FTO-SnO₂-Fe₂O₃ film indicates increased charge separation and thus reduced electron–hole recombination at the substrate/hematite interface. Such an effect would be beneficial for the electrochemical reaction of holes at the SCLJ. For the further elucidation of the origin of this interface effect, electronic structure analysis of the substrate/hematite interface was performed with XPS and NEXAFS spectroscopy.

XPS is a predominantly surface-sensitive technique⁴³ which can produce molecular and electronic structure information at and beneath the electrode surface. The electronic structure at the hematite–substrate interface can only be probed directly if it exists within the inelastic mean free path of electrons generated by X-ray irradiation. For this reason, we have deposited wedge-shaped α -Fe₂O₃ thin films with gradient thickness on FTO and FTO–SnO₂ substrates. The FTO layer, SnO₂ film, and Fe₂O₃ film are not compact layers but porous films. The α -Fe₂O₃ film wedge thickness thus ranged from 0 to 100 nm over the 8 mm length over the substrate. Note that the beam spot size is 500 μ m, over which the height thus changes by 6.25 nm. We scanned the X-ray beam from the hematite-free area to the hematite-rich area until both signals from the α -Fe₂O₃ film and substrate were clearly observed, confirming that we had identified the substrate/ α -Fe₂O₃ interface. This is illustrated in the visual experiment summary and the XPS survey scan spectra in Figure 3. Peaks at binding energies of 56,

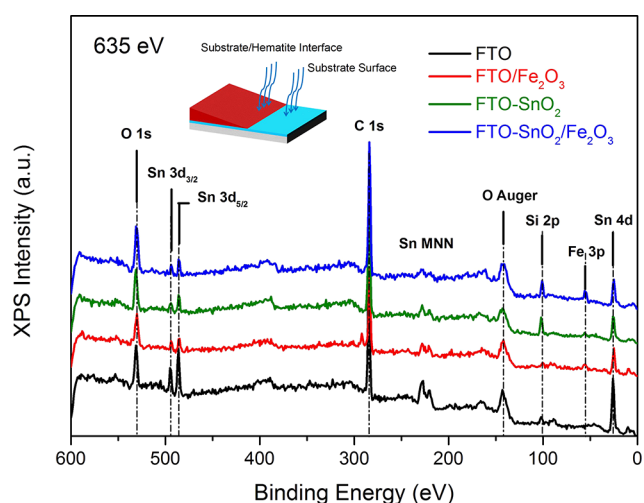


Figure 3. X-ray photoelectron spectroscopy survey scan for (ordered bottom to top) FTO surface, FTO/Fe₂O₃ interface, FTO–SnO₂ surface, and FTO–SnO₂/Fe₂O₃ interface. The excitation energy was 635 eV. The image on the top denotes the wedge-shaped iron oxide film in red with 100 nm thickness on the far end and 0 nm at the blue substrate surface.

487, and 495 eV, which correspond to Fe 3p from α -Fe₂O₃ and to Sn 3d_{3/2} and 3d_{5/2} from the substrate, are observed in the FTO/ α -Fe₂O₃ and FTO–SnO₂/ α -Fe₂O₃ interface, indicating that the substrate/hematite interfaces were indeed probed. In addition to adventitious carbon (C 1s peak), which can hardly be avoided on porous materials, we also notice a Si 2p peak, which is likely a result of interdiffusion of Si from the FTO glass substrate during annealing. The FTO spectrum (black) shows, as expected, no peak from Fe at 56 eV, whereas the spectrum recorded on the wedge (blue spectrum) shows a clear Fe signature. Also, the spectrum of the FTO–Fe₂O₃ sample (red spectrum) shows a noticeable yet very weak such Fe peak. The spectrum (green) recorded at the FTO–SnO₂ region shows at 56 eV a spurious intensity which might be attributed to the width of the X-ray beam having probed part of the Fe₂O₃ wedge.

Figure 4 shows in three panels the oxygen core level (O 1s) XPS spectra of the FTO surface, FTO/ α -Fe₂O₃ interface, FTO–SnO₂ surface, and FTO–SnO₂/ α -Fe₂O₃ interface. At first glance, we notice a convoluted double-peak structure for

all spectra, which originates from oxygen near the metal ion and from hydroxyl ions. We have recently investigated the oxygen spectra of iron oxide photoelectrodes and identified two marker peaks for structural oxygen O_{Fe} in Fe₂O₃ and O₂^{2–} from OH[–] (see Figure 6 in ref 44). The spectra shown here are convoluted with the oxygen XPS signatures from the oxygen atoms in FTO and SnO₂ and therefore difficult to extract. The decomposition of the entire O 1s peak was performed by least-squares fitting using Gauss–Lorentz functions. The O 1s peaks for FTO and FTO–SnO₂ surface were deconvoluted into two overlapping peaks: one at lower binding energy, around 530.6 eV, which is attributed to structural oxygen in SnO₂ or F-doped SnO₂, and another peak at the left at higher binding energy, around 532.2 eV, which originates from adsorbed hydroxide and/or oxyhydroxide species.

The peak around 532.2 eV is clearly wider with a larger FWHM value, suggesting that it may include an additional unresolved component, for example adsorbed oxygen O[–] or O₂^{2–}.⁴⁵ Differences between O1s spectra for substrate surface (FTO and FTO–SnO₂ surface) and substrate/hematite interface (FTO/ α -Fe₂O₃ and FTO–SnO₂/ α -Fe₂O₃ interface) are observed due to the contribution of α -Fe₂O₃ (see the right panel in Figure 4). The peak at around 530.1 eV (O_{Fe}) originates from structural oxygen in α -Fe₂O₃, and the peak at around 531.6 eV (O₂^{2–}) is due to surface functional hydroxyl groups (compare refs 46–48). We have made a similar observation with ambient pressure XPS on ceramic proton conductors⁴⁹ and on iron oxide nanoparticles.⁴⁸ One may pose the question whether the enhanced presence of the surface functional hydroxyl groups has an influence on the PEC performance. While we have no satisfactory answer to this, the PEC performance certainly is better as is shown in the data. The increased presence of hydroxyl groups might be a secondary effect. We do know that the concentration of hydroxyl groups on the surface is linear increasing with bias potential until the water splitting onset potential is reached.⁵⁰ From that point on the concentration decreases again.⁵⁰ But this is not the scope of the current work.

Close inspection of the two spectra on the right panel in Figure 4 shows that the oxygen spectrum shifts to somewhat higher binding energy by 180 meV, when the SnO₂ buffer layer is introduced. This shift could be a shift in the binding energy and originate from the change in the surface potential because it correlates with a change in the work function by the same order of magnitude, i.e., 130 meV. Confirmation of this scenario would require, however, that we compare the binding energy of the Fe core level or the valence band spectra.

An alternative explanation for the observed broadening of the peak at the higher binding energy is that this is not a shift of the entire spectrum but a gain of additional spectral weight at the high-energy part of the spectrum from 532 to 534 eV. The solid lines through the data points are weighted averaged data. To quantify this effect, we have determined the center of gravity (first statistical moment) $\langle E \rangle$ of both spectra according to the relation⁵¹

$$\langle E \rangle = \frac{\int I(E)E \, dE}{\int I(E) \, dE}$$

which yields 531.47 and 531.54 eV, respectively. This amounts to a spectral difference for $\langle E \rangle$ of 70 meV.

The intensity at 532 eV (here: 532.2 eV) is frequently interpreted as the signature of oxygen vacancies.⁵² Because

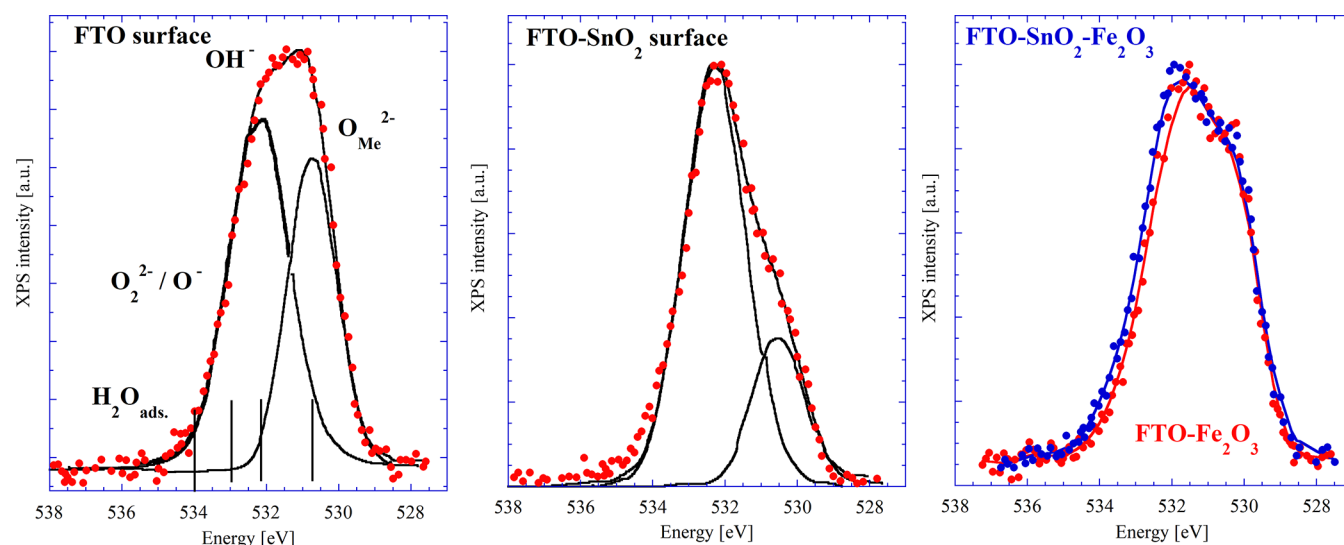


Figure 4. O 1s XPS spectra with deconvolution for (left) FTO surface, (middle) FTO–SnO₂ surface, (right) FTO/Fe₂O₃ interface (red), and FTO–SnO₂/Fe₂O₃ interface (blue). Filled symbols are the data points. Solid lines are least-squares fits. The O 1s peak deconvolutions were made by using Gauss–Lorentz product functions. The photon energy was 635 eV.

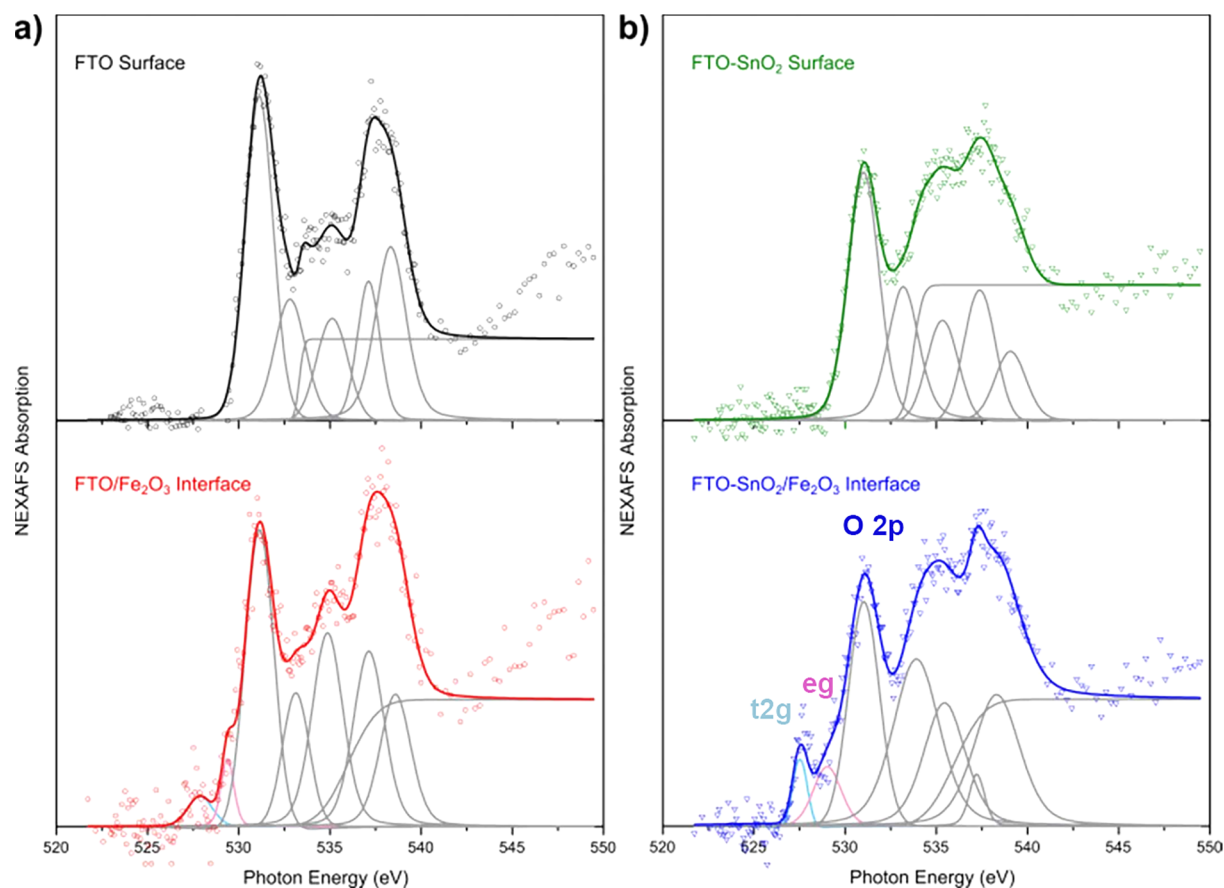


Figure 5. O K-edge spectra and deconvoluted spectra for (a) FTO surface (black), FTO/Fe₂O₃ interface (red) and (b) FTO–SnO₂ surface (olive), FTO–SnO₂/Fe₂O₃ interface (blue).

oxygen vacancies cannot emit photoelectrons, the correct description is that the peak originates from oxygen in an oxygen-deficient environment in solids. We have recently shown that the surface of our as-prepared α -Fe₂O₃ iron oxide photoelectrodes is oxygen-deficient and terminated with Fe²⁺,^{44,53} which is known to catalyze the water splitting reaction.⁵⁴ Oxidation of the photoelectrode surface by

anodization in KOH can “heal” the defect states from Fe²⁺, as it becomes oxidized to Fe³⁺. Actual confirmation of the presence of Fe²⁺ at the surface could directly be proven by the Fe core level or the valence band spectra, the latter of which we confirmed recently in a separate study.^{44,53} In a previous study on tungsten oxide (nominally WO₃) thin films pulsed laser deposited on TiO₂, we found defect states from “blue color”

oxygen-deficient tungsten oxide on the surface and in the interface between tungsten oxide and TiO_2 substrate. The former were healed by thermal gas phase oxidation, whereas the latter seemed to resist such an attempt.^{55,56}

We have confidence that the XPS results insofar suggest that the improved water oxidation performance upon buffer layer engineering is associated with the change of the electronic structure of interface formed between hematite and substrate. We share, however, the concerns of two anonymous reviewers and have no doubt that a further improved design of the electrode assembly, for example by studying pulsed laser deposited compact films and measuring with core level spectroscopy and resonant photoemission spectroscopy or hard X-ray XPS,⁵⁷ would raise our confidence.

NEXAFS spectroscopy is highly sensitive to the local molecular structure of the atom absorbing the X-rays. The O K-edge absorption spectra represent the O 2p unoccupied density-of-states and thus provide information about interfacial metal sites relevant to hybridization of metal weight and O 2p character. Figure 5 displays the O K-edge NEXAFS spectra and their deconvoluted spectra for substrate surfaces and substrate–hematite interfaces. While the statistical significance of the spectra does not allow for an accurate deconvolution, we show for the reader suggested deconvolution based on the known molecular orbitals of hematite,⁵⁸ as exercised in our recent paper.⁵⁹ Voigt functions are utilized for deconvolution. The spectra in the top panel of Figure 5 present the normalized total electron yields generated upon irradiation of FTO and FTO– SnO_2 surfaces.

The spectra have a strong resonance at 531.2 eV, representing the hybridization of the O 2p and Sn 5s orbital of SnO_2 or FTO.⁶⁰ The set of features at high photon energy from 532 to 540 eV are a composite of the O 2p weights in the Sn 5p orbitals. These are in good agreement with our previously reported study on FTO.⁶¹ The bottom two plots show the O K-edge NEXAFS spectra for FTO/ $\alpha\text{-Fe}_2\text{O}_3$ and FTO– SnO_2 / $\alpha\text{-Fe}_2\text{O}_3$ interfaces. The envelope spectra are the sum of the signals from $\alpha\text{-Fe}_2\text{O}_3$ and SnO_2 . These spectra have a pre-edge feature below 530 eV, which is absent in the spectrum of FTO and the FTO– SnO_2 surface and thus should be the signature of the ferric oxide. This feature usually appears as a doublet in $\alpha\text{-Fe}_2\text{O}_3$, which represents unoccupied O 2p states hybridized with the Fe 3d band, predominantly localizing around metal-atom sites: t_{2g} centered at 527.6 eV and e_g centered at 529.1 eV—indicative to $\alpha\text{-Fe}_2\text{O}_3$. The separation of these two orbitals is related to the crystal-field splitting of $\alpha\text{-Fe}_2\text{O}_3$. We observe that the relative spectral weight of the t_{2g} peak increases—with respect to the e_g shoulder and the O 2p peak—when the SnO_2 buffer layer is introduced. Along with the increase of the t_{2g} signature, in Figure 5, we notice a considerable increase of intensity of the shoulder right next to the e_g peak. We found recently that the exposure of pristine dry $\alpha\text{-Fe}_2\text{O}_3$ photoelectrode to aqueous electrolyte—this was an *operando in situ* experiment with an X-ray spectrophotocatalytic cell⁵⁹—causes an enhancement of the t_{2g} peak relative to the e_g peak (compare Figure 3, left panel, in ref 50). We know from previous studies that pristine $\alpha\text{-Fe}_2\text{O}_3$ tends to be substoichiometric at the surface.^{44,53} Our interpretation was that the pristine $\alpha\text{-Fe}_2\text{O}_3$ is oxygen-deficient at the surface, indicated by a lower intensity t_{2g} peak, and subsequent exposure to the H_2O molecules might fill these oxygen vacancies and shift up the intensity of the smaller t_{2g} peak. We make a similar observation in this study,

where upon insertion of the buffer layer, a hitherto low-intensity t_{2g} peak in $\alpha\text{-Fe}_2\text{O}_3$ increases noticeably. It is therefore possible that the SnO_2 buffer layer has the effect on $\alpha\text{-Fe}_2\text{O}_3$ that it is less oxygen deficient at the SnO_2 – $\alpha\text{-Fe}_2\text{O}_3$ interface. We therefore included in the two concerned spectra in Figure 5 two additional Voigt functions for its deconvolution in the pre-edge range for the spectra of substrate/hematite interface, shown as blue line for t_{2g} and red for e_g .

While the statistics of the data points at this pre-edge structure of the O K-edge NEXAFS are too poor for accurate determination of a fine structure that goes beyond the established t_{2g} – e_g doublet, the scattering of the actual data points suggests there is a difference in the width of the spectral distribution of intensity. We then wish to compare the least-squares-fit lines of the spectra in the relevant energy region. Therefore, the analysis that follows must be taken with a grain of salt; but we feel the speculation is worthwhile to be pursued because the results from electroanalytical techniques turn out to match the results from the X-ray spectroscopy. This would warrant further investigation by the community.

We have normalized both deconvoluted spectra from the iron containing electrodes to the t_{2g} peak intensity to compare them, as shown in Figure 6. We are comparing here the least-

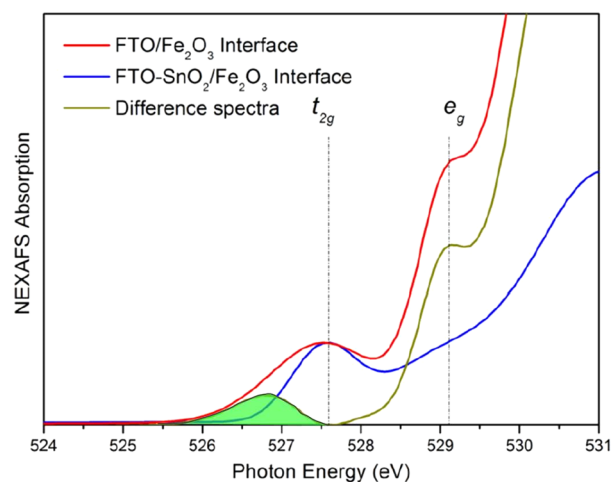


Figure 6. Least-squares fits of the O K-edge difference spectra of FTO– Fe_2O_3 (red) and FTO– SnO_2 – Fe_2O_3 (blue) and difference spectrum (dark yellow) obtained by subtraction of FTO– Fe_2O_3 spectra from FTO– SnO_2 – Fe_2O_3 spectra. For this comparison, spectra are normalized at the energy position of the t_{2g} at 527.6 eV.

squares fits to the spectra and notice that the spectrum from the FTO– Fe_2O_3 interface is broader in the t_{2g} region than the one with the SnO_2 buffer layer in between. The difference of the interfacial Fe 3d band due to the SnO_2 buffer layer is reflected in the difference spectra in Figure 6 obtained by subtraction of the FTO– $\alpha\text{-Fe}_2\text{O}_3$ spectra from the FTO– SnO_2 / $\alpha\text{-Fe}_2\text{O}_3$ spectra. The interface of $\alpha\text{-Fe}_2\text{O}_3$ with FTO is associated with a distribution of unoccupied O 2p states located below the lowest unoccupied Fe 3d orbitals, emerging from the displacement of Fe^{3+} ions in the corundum structure in $\alpha\text{-Fe}_2\text{O}_3$.²³ It can be represented by the feature below the t_{2g} peak, centered at around 526.9 eV.

The positive intensity of this peak in the difference spectra at this region indicates the elimination of these electronic states by the SnO_2 buffer layer. Previous studies on the FTO– α -

Fe_2O_3 interface indicated a reduction of the degree of p–d orbital hybridization due to the interaction of $\alpha\text{-Fe}_2\text{O}_3$ with FTO.²³ We also observe in our sample on the FTO– $\alpha\text{-Fe}_2\text{O}_3$ interface a broadening of Fe 3d–O 2p hybridized states. The feature of the difference spectra near 528.4 eV, located between the t_{2g} and e_g peaks, shows a positive value, suggesting an enhancement of the crystal-field splitting of $\alpha\text{-Fe}_2\text{O}_3$ on FTO– SnO_2 and an improvement on the degree of p–d orbital hybridization. A broadening or an absence of observable splitting of t_{2g} and e_g peaks may arise from the multiplicity of oxygen states, which may relate to size effects and structural distortion.^{62,63} For $\alpha\text{-Fe}_2\text{O}_3$ on FTO with smaller feature size, it is reasonable to postulate that a high density of states and the presence of imperfections and strain anisotropies of the sample may result in a distortion and site inequivalence of the oxygen octahedral sites surrounding the iron ion. In addition, the straining of the FTO– $\alpha\text{-Fe}_2\text{O}_3$ film may shorten the metal–ligand distance and cause a low t_{2g}/e_g peak ratio, the value of which was then increased by the structural relaxation effect from the SnO_2 layer.

Upon comparison of the spectra in Figure 6, the data indicate that shifts of the conduction band edge energy and density-of-states result from the electronic interaction of $\alpha\text{-Fe}_2\text{O}_3$ with the substrate. It should be possible for us to use these parameters for the determination of the quasi-Fermi level of electrons in a semiconductor by⁶⁴

$$E_{\text{Fn}}(x) = E_{\text{cb}}(x) + kT \ln \left\{ \frac{n(x)}{N_c} \right\}$$

where $E_{\text{cb}}(x)$ is the electrical potential energy of the conduction band edge, n is the concentration of electrons, and N_c is the density of electronic states at the bottom of the conduction band. This would further alter the flat-band potential of the deposited hematite, which is intimately related to the quasi-Fermi level of electrons in the photoanode. We can access the flat-band potential with electroanalytical techniques such as impedance spectroscopy when we vary the bias potential and record the capacity of the subsurface (we call it for simplicity C_{bulk}) versus the DC bias in a Mott–Schottky plot (Figure 7). The thus-determined space charge

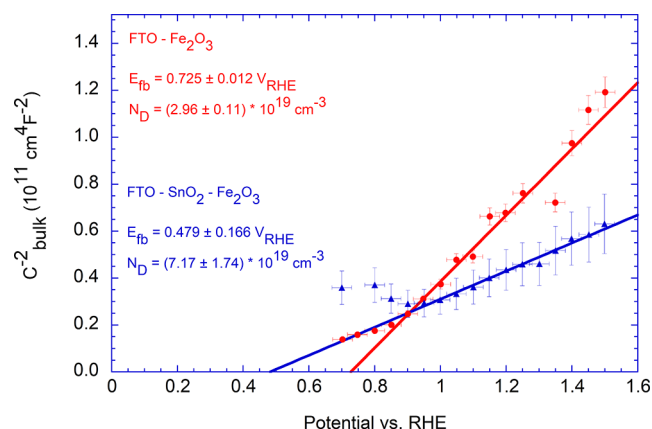


Figure 7. Comparison of the Mott–Schottky plots of FTO– Fe_2O_3 (red bullets) and FTO– SnO_2 – Fe_2O_3 (blue triangles) samples in the dark condition. Solid lines are linear least-squares fits. Upon adding the SnO_2 buffer layer, the flat-band potential E_{fb} lowers from 0.725 to 0.479 V vs RHE. The charge carrier concentration N_D increases by a factor of >2 from 2.96×10^{19} to $7.17 \times 10^{19} \text{ per cm}^3$.

capacitance contribution of the subsurface can be plotted as C_{bulk}^{-2} vs the bias potential and yields from the intercept a flat-band potential of 0.73 V for the hematite on FTO and 0.49 V for the electrode when the buffer layer is put in-between (i.e., a shift of 240 mV toward lower potential). The inverse slope yields the charge carrier (donor) concentration, which increases from 2.9×10^{19} to $7 \times 10^{19} \text{ cm}^{-3}$ when the buffer layer is introduced.

The aforementioned NEXAFS data provide the electronic structure rational for the improved performance by the SnO_2 buffer layer.

CONCLUSIONS

We have explained the function of the SnO_2 buffer layer, which is used to enhance the PEC performance of hematite films. The hematite film with SnO_2 buffer layer exhibited a cathodic shift of onset potential by 180 mV, and a shift of the work function by 130 mV, and improved photocurrent density at 1.23 V vs RHE to 0.45 mA/cm^2 . The lifetime of charge carriers was enhanced by a factor of more than 10. GIXRD reveals that the buffer layer contributes to an alteration of the nucleation and growth mode of hematite films, enabling a better crystallinity and conformal coating on the substrate. The principal function of the buffer layer was attributed to diminishing oxygen vacancies in the deposited hematite and to eliminate unoccupied oxygen p-hybridized states on the substrate/ $\alpha\text{-Fe}_2\text{O}_3$ interface. The interaction of $\alpha\text{-Fe}_2\text{O}_3$ with FTO has been decreased as expressed in the observed splitting of Fe 3d–O 2p hybridized states and thus enhanced degree of p–d orbital hybridization. These findings highlight that the composition and structure of metal oxide as buffer layer can be engineered with better electrical functionality in solar water splitting photoelectrodes. An improvement of the electrode assembly architecture for analytical purposes, such as more homogeneous and compact films, an improved metrology, and use of element specific X-ray spectroscopy methods, could better pinpoint the suggestions made in this study. Maybe this article gives inspiration to researchers in related communities for addressing this issue.

AUTHOR INFORMATION

Corresponding Author

Artur Braun – Laboratory for High Performance Ceramics, Empa - Swiss Federal Laboratories for Materials Science and Technology, CH-8600 Dübendorf, Switzerland;
orcid.org/0000-0002-6992-7774; Email: artur.braun@alumni.ethz.ch

Authors

Yelin Hu – Laboratory for High Performance Ceramics, Empa - Swiss Federal Laboratories for Materials Science and Technology, CH-8600 Dübendorf, Switzerland; Laboratory for Photonics and Interfaces, Swiss Federal Institute of Technology (EPFL), CH-1015 Lausanne, Switzerland
Florent Boudoire – Laboratory for High Performance Ceramics, Empa - Swiss Federal Laboratories for Materials Science and Technology, CH-8600 Dübendorf, Switzerland; Department of Chemistry, University of Basel, CH-4056 Basel, Switzerland
Matthew T. Mayer – Laboratory for Photonics and Interfaces, Swiss Federal Institute of Technology (EPFL), CH-1015 Lausanne, Switzerland

Songhak Yoon – Laboratory for High Performance Ceramics, Empa - Swiss Federal Laboratories for Materials Science and Technology, CH-8600 Dübendorf, Switzerland

Michael Graetzel – Laboratory for Photonics and Interfaces, Swiss Federal Institute of Technology (EPFL), CH-1015 Lausanne, Switzerland; orcid.org/0000-0002-0068-0195

Complete contact information is available at:
<https://pubs.acs.org/10.1021/acs.jpcc.1c01809>

Notes

The authors declare no competing financial interest.

ACKNOWLEDGMENTS

Financial support by the Swiss National Science Foundation project no. 200021-132126 (Y.H.), R'equip no. 206021-121306, NanoTera SHINE no. 20NA21-145936, and Indo Swiss Joint Research Program (S.Y.) IZLIZ2-138864 is acknowledged. The authors thank Jianjun Wang and Thomas Moehl for helpful discussions and Jianshan Luo and David Tilley for their help on ALD. M.T.M. and M.G. acknowledge support from the Swiss Federal Office of Energy under the PECHouse project. The Advanced Light Source is supported by the Director, Office of Science, Office of Basic Energy Sciences, of the U.S. Department of Energy under Contract DE-AC02-05CH11231.

REFERENCES

- (1) Kennedy, J. H.; Frese, K. W. Photooxidation of Water at α -Fe₂O₃ Electrodes. *J. Electrochem. Soc.* **1978**, *125* (5), 709–714.
- (2) Balberg, I.; Pinch, H. L. Optical-Absorption of Iron-Oxides. *J. Magn. Mater.* **1978**, *7* (1–4), 12–15.
- (3) Kayes, B. M.; Atwater, H. A.; Lewis, N. S. Comparison of the Device Physics Principles of Planar and Radial p-n Junction Nanorod Solar Cells. *J. Appl. Phys.* **2005**, *97* (11), 114302.
- (4) Stefk, M.; Cornuz, M.; Mathews, N.; Hisatomi, T.; Mhaisalkar, S.; Grätzel, M. Transparent, Conducting Nb:SnO₂ for Host–Guest Photoelectrochemistry. *Nano Lett.* **2012**, *12* (10), 5431–5435.
- (5) Sivula, K.; Formal, F. L.; Grätzel, M. WO₃–Fe₂O₃ Photoanodes for Water Splitting: A Host Scaffold, Guest Absorber Approach. *Chem. Mater.* **2009**, *21* (13), 2862–2867.
- (6) Lin, Y.; Zhou, S.; Sheehan, S. W.; Wang, D. Nanonet-Based Hematite Heteronanostructures for Efficient Solar Water Splitting. *J. Am. Chem. Soc.* **2011**, *133* (8), 2398–2401.
- (7) Boudoire, F.; Toth, R.; Heier, J.; Braun, A.; Constable, E. C. Photonic Light Trapping in Self-Organized All-Oxide Microspheroids Impacts Photoelectrochemical Water Splitting. *Energy Environ. Sci.* **2014**, *7* (8), 2680–2688.
- (8) Brillet, J.; Grätzel, M.; Sivula, K. Decoupling Feature Size and Functionality in Solution-Processed, Porous Hematite Electrodes for Solar Water Splitting. *Nano Lett.* **2010**, *10* (10), 4155–4160.
- (9) Shen, S.; Zhou, J.; Dong, C.-L.; Hu, Y.; Tseng, E. N.; Guo, P.; Guo, L.; Mao, S. S. Surface Engineered Doping of Hematite Nanorod Arrays for Improved Photoelectrochemical Water Splitting. *Sci. Rep.* **2015**, *4*, 6627.
- (10) Sivula, K.; Zboril, R.; Le Formal, F.; Robert, R.; Weidenkaff, A.; Tucek, J.; Frydrych, J.; Grätzel, M. Photoelectrochemical Water Splitting with Mesoporous Hematite Prepared by a Solution-Based Colloidal Approach. *J. Am. Chem. Soc.* **2010**, *132* (21), 7436–7444.
- (11) Hisatomi, T.; Brillet, J.; Cornuz, M.; Le Formal, F.; Tetreault, N.; Sivula, K.; Grätzel, M. A Ga₂O₃ underlayer as an isomorphic template for ultrathin hematite films toward efficient photoelectrochemical water splitting. *Faraday Discuss.* **2012**, *155*, 223–232.
- (12) Hisatomi, T.; Dotan, H.; Stefk, M.; Sivula, K.; Rothschild, A.; Grätzel, M.; Mathews, N. Enhancement in the Performance of Ultrathin Hematite Photoanode for Water Splitting by an Oxide Underlayer. *Adv. Mater.* **2012**, *24* (20), 2699–2702.
- (13) Hisatomi, T.; Le Formal, F.; Cornuz, M.; Brillet, J.; Tetreault, N.; Sivula, K.; Grätzel, M. Cathodic Shift in Onset Potential of Solar Oxygen Evolution on Hematite by 13-group Oxide Overlayers. *Energy Environ. Sci.* **2011**, *4* (7), 2512–2515.
- (14) Le Formal, F.; Grätzel, M.; Sivula, K. Controlling Photoactivity in Ultrathin Hematite Films for Solar Water-Splitting. *Adv. Funct. Mater.* **2010**, *20* (7), 1099–1107.
- (15) Lopes, T.; Andrade, L.; Le Formal, F.; Grätzel, M.; Sivula, K.; Mendes, A. Hematite Photoelectrodes for Water Splitting: Evaluation of The Role of Film Thickness by Impedance Spectroscopy. *Phys. Chem. Chem. Phys.* **2014**, *16* (31), 16515–16523.
- (16) Yang, X.; Liu, R.; Du, C.; Dai, P.; Zheng, Z.; Wang, D. Improving Hematite-based Photoelectrochemical Water Splitting with Ultrathin TiO₂ by Atomic Layer Deposition. *ACS Appl. Mater. Interfaces* **2014**, *6* (15), 12005–12011.
- (17) Klahr, B. M.; Hamann, T. W. Current and Voltage Limiting Processes in Thin Film Hematite Electrodes. *J. Phys. Chem. C* **2011**, *115* (16), 8393–8399.
- (18) Riha, S. C.; Klahr, B. M.; Tyo, E. C.; Seifert, S.; Vajda, S.; Pellin, M. J.; Hamann, T. W.; Martinson, A. B. F. Atomic Layer Deposition of a Submonolayer Catalyst for the Enhanced Photoelectrochemical Performance of Water Oxidation with Hematite. *ACS Nano* **2013**, *7* (3), 2396–2405.
- (19) Zandi, O.; Hamann, T. W. Enhanced Water Splitting Efficiency Through Selective Surface State Removal. *J. Phys. Chem. Lett.* **2014**, *5* (9), 1522–1526.
- (20) Hamd, W.; Cobo, S.; Fize, J.; Baldinozzi, G.; Schwartz, W.; Reymermier, M.; Pereira, A.; Fontecave, M.; Artero, V.; Laberty-Robert, C.; et al. Mesoporous α -Fe₂O₃ Thin Films Synthesized via the Sol-Gel Process for Light-Driven Water Oxidation. *Phys. Chem. Chem. Phys.* **2012**, *14* (38), 13224–13232.
- (21) Herrmann-Geppert, I.; Bogdanoff, P.; Fengler, S.; Dittrich, T.; Fiechter, S. Photoelectrooxidation of Water on Hematite Thin Films. In *Fullerenes, Nanotubes, and Carbon Nanostructures - 221st Ecs Meeting*; Guldi, D. M., Fenton, J. M., Simonian, A., Eds.; 2013; Vol. 45, pp 137–147.
- (22) Itoh, K.; Bockris, J. O. M. Thin Film Photoelectrochemistry: Iron Oxide. *J. Electrochem. Soc.* **1984**, *131* (6), 1266–1271.
- (23) Kronawitter, C. X.; Zegkinoglou, I.; Rogero, C.; Guo, J. H.; Mao, S. S.; Himpel, F. J.; Vayssieres, L. On the Interfacial Electronic Structure Origin of Efficiency Enhancement in Hematite Photoanodes. *J. Phys. Chem. C* **2012**, *116* (43), 22780–22785.
- (24) Pailhé, N.; Wattiaux, A.; Gaudon, M.; Demourgues, A. Impact of Structural Features on Pigment Properties of α -Fe₂O₃ Hematite. *J. Solid State Chem.* **2008**, *181* (10), 2697–2704.
- (25) Zandi, O.; Beardslee, J. A.; Hamann, T. Substrate Dependent Water Splitting with Ultrathin α -Fe₂O₃ Electrodes. *J. Phys. Chem. C* **2014**, *118* (30), 16494–16503.
- (26) Kondofersky, I.; Dunn, H. K.; Müller, A.; Mandlmeier, B.; Feckl, J. M.; Fattakhova-Rohlfing, D.; Scheu, C.; Peter, L. M.; Bein, T. Electron Collection in Host–Guest Nanostructured Hematite Photoanodes for Water Splitting: The Influence of Scaffold Doping Density. *ACS Appl. Mater. Interfaces* **2015**, *7* (8), 4623–4630.
- (27) Wang, L.; Palacios-Padrós, A.; Kirchgeorg, R.; Tighineanu, A.; Schmuki, P. Enhanced Photoelectrochemical Water Splitting Efficiency of a Hematite–Ordered Sb:SnO₂ Host–Guest System. *ChemSusChem* **2014**, *7* (2), 421–424.
- (28) Kay, A.; Cesar, I.; Graetzel, M. New Benchmark for Water Photooxidation by Nanostructured α -Fe₂O₃ Films. *J. Am. Chem. Soc.* **2006**, *128* (49), 15714–15721.
- (29) Ter Minassian-Sarag, L.; Vincent, B.; Adler, M.; Barraud, A.; Churaev, N. V.; Eaton, D. F.; Kuhn, H.; Misono, M.; Platanov, D.; Ralston, J.; Silberberg, A.; Zemel, J. N. Thin films including layers: Terminology in relation to their preparation and characterization - IUPAC Recommendations 1994. *Thin Solid Films* **1996**, *277* (1–2), 7–78.
- (30) Kuroiwa, K.; Aoki, T.; Fujimoto, M. Electrical Properties of GaAs Vapor Phase Epitaxial Layers. *J. Cryst. Growth* **1974**, *24*, 229–232.

- (31) Zhang, C.; Wu, Q.; Ke, X.; Wang, J.; Jin, X.; Xue, S. Ultrathin Hematite Films Deposited Layer-by-Layer on a TiO_2 Underlayer for Efficient Water Splitting Under Visible Light. *Int. J. Hydrogen Energy* **2014**, *39* (27), 14604–14612.
- (32) Wang, D.; Zhang, X.-T.; Sun, P.-P.; Lu, S.; Wang, L.-L.; Wei, Y.-A.; Liu, Y.-C. Enhanced Photoelectrochemical Water Splitting on Hematite Thin Film with Layer-by-Layer Deposited Ultrathin TiO_2 Underlayer. *Int. J. Hydrogen Energy* **2014**, *39* (28), 16212–16219.
- (33) Liang, Y. Q.; Enache, C. S.; van de Krol, R. Photoelectrochemical Characterization of Sprayed $\alpha\text{-Fe}_2\text{O}_3$ Thin Films: Influence of Si Doping and SnO_2 Interfacial Layer. *Int. J. Photoenergy* **2008**, *2008*, 1–7.
- (34) Steier, L.; Herraiz-Cardona, I.; Gimenez, S.; Fabregat-Santiago, F.; Bisquert, J.; Tilley, S. D.; Grätzel, M. Understanding the Role of Underlayers and Overlayers in Thin Film Hematite Photoanodes. *Adv. Funct. Mater.* **2014**, *24* (48), 7681–7688.
- (35) Le Formal, F.; Tetreault, N.; Cornuz, M.; Moehl, T.; Grätzel, M.; Sivula, K. Passivating Surface States on Water Splitting Hematite Photoanodes with Alumina Overlayers. *Chemical Science* **2011**, *2* (4), 737–743.
- (36) Murthy, A. S. N.; Reddy, K. S. Photoelectrochemical Behavior of Undoped ferric-oxide ($\alpha\text{-Fe}_2\text{O}_3$) Electrodes Prepared by Spray Pyrolysis. *Mater. Res. Bull.* **1984**, *19* (2), 241–246.
- (37) Chen, Z.; Jaramillo, T. F.; Deutsch, T. G.; Kleiman-Shwarsstein, A.; Forman, A. J.; Gaillard, N.; Garland, R.; Takanabe, K.; Heske, C.; Sunkara, M.; et al. Accelerating Materials Development for Photoelectrochemical Hydrogen Production: Standards for Methods, Definitions, and Reporting Protocols. *J. Mater. Res.* **2010**, *25* (01), 3–16.
- (38) Tafalla, D.; Salvador, P.; Benito, R. M. Kinetic Approach to the Photocurrent Transients in Water Photoelectrolysis at n- TiO_2 Electrodes: II. Analysis of the Photocurrent-Time Dependence. *J. Electrochem. Soc.* **1990**, *137* (6), 1810–1815.
- (39) Dareedwards, M. P.; Goodenough, J. B.; Hamnett, A.; Trevellick, P. R. Electrochemistry and Photoelectrochemistry of Iron(III) Oxide. *J. Chem. Soc., Faraday Trans. 1* **1983**, *79*, 2027–2041.
- (40) Iwanski, P.; Curran, J. S.; Gissler, W.; Memming, R. The Photoelectrochemical Behavior of Ferric Oxide in the Presence of Redox Reagents. *J. Electrochem. Soc.* **1981**, *128* (10), 2128–2133.
- (41) Cesar, I.; Sivula, K.; Kay, A.; Zboril, R.; Grätzel, M. Influence of Feature Size, Film Thickness, and Silicon Doping on the Performance of Nanostructured Hematite Photoanodes for Solar Water Splitting. *The J. Phys. Chem. C* **2009**, *113* (2), 772–782.
- (42) Sivula, K.; Zboril, R.; Le Formal, F.; Robert, R.; Weidenkaff, A.; Tucek, J.; Frydrych, J.; Grätzel, M. Photoelectrochemical Water Splitting with Mesoporous Hematite Prepared by a Solution-Based Colloidal Approach. *J. Am. Chem. Soc.* **2010**, *132* (21), 7436–7444.
- (43) Seah, M. P.; Dench, W. A. Quantitative Electron Spectroscopy of Surfaces: A Standard Data Base for Electron Inelastic Mean Free Paths in Solids. *Surf. Interface Anal.* **1979**, *1* (1), 2–11.
- (44) Braun, A.; Chen, Q.; Flak, D.; Fortunato, G.; Gajda-Schranz, K.; Grätzel, M.; Graule, T.; Guo, J.; Huang, T. W.; Liu, Z.; et al. Iron resonant photoemission spectroscopy on anodized hematite points to electron hole doping during anodization. *ChemPhysChem* **2012**, *13* (12), 2937–44.
- (45) Kawabe, T.; Shimomura, S.; Karasuda, T.; Tabata, K.; Suzuki, E.; Yamaguchi, Y. Photoemission Study of Dissociatively Adsorbed Methane on a Pre-Oxidized SnO_2 Thin Film. *Surf. Sci.* **2000**, *448* (2–3), 101–107.
- (46) Flak, D.; Braun, A.; Mun, B. S.; Döbeli, M.; Graule, T.; Rekas, M. Electronic structure and surface properties of nonstoichiometric $\text{Fe}_2\text{O}_3\text{-}\delta$ (α and γ) and its application in gas Sensing. *Procedia Eng.* **2012**, *47*, 257–260.
- (47) Flak, D.; Braun, A.; Mun, B. S.; Park, J. B.; Parlinska-Wojtan, M.; Graule, T.; Rekas, M. Spectroscopic assessment of the role of hydrogen in surface defects, in the electronic structure and transport properties of TiO_2 , ZnO and SnO_2 nanoparticles. *Phys. Chem. Chem. Phys.* **2013**, *15* (5), 1417–30.
- (48) Flak, D.; Chen, Q. L.; Mun, B. S.; Liu, Z.; Rekas, M.; Braun, A. In situ ambient pressure XPS observation of surface chemistry and electronic structure of $\alpha\text{-Fe}_2\text{O}_3$ and $\gamma\text{-Fe}_2\text{O}_3$ nanoparticles. *Appl. Surf. Sci.* **2018**, *455*, 1019–1028.
- (49) Chen, Q.; El Gabaly, F.; Akgul, F. A.; Liu, Z.; Mun, B. S.; Yamaguchi, S.; Braun, A. Observation of Oxygen Vacancy Filling under Water Vapor in Ceramic Proton Conductors in Situ with Ambient Pressure XPS. *Chem. Mater.* **2013**, *25* (23), 4690–4696.
- (50) Braun, A.; Hu, Y.; Boudoire, F.; Bora, D. K.; Sarma, D. D.; Graetzel, M.; Eggleston, C. M. The electronic, chemical and electrocatalytic processes and intermediates on iron oxide surfaces during photoelectrochemical water splitting. *Catal. Today* **2016**, *260*, 72–81.
- (51) Braun, A.; Wang, H.; Bergmann, U.; Tucker, M. C.; Gu, W.; Cramer, S. P.; Cairns, E. J. Origin of chemical shift of manganese in lithium battery electrode materials—a comparison of hard and soft X-ray techniques. *J. Power Sources* **2002**, *112* (1), 231–235.
- (52) Jain, S.; Shah, J.; Negi, N. S.; Sharma, C.; Kotnala, R. K. Significance of interface barrier at electrode of hematite hydroelectric cell for generating ecopower by water splitting. *Int. J. Energy Res.* **2019**, *43* (9), 4743–4755.
- (53) Gajda-Schranz, K.; Tymen, S.; Boudoire, F.; Toth, R.; Bora, D. K.; Calvet, W.; Grätzel, M.; Constable, E. C.; Braun, A. Formation of an electron hole doped film in the $\alpha\text{-Fe}_2\text{O}_3$ photoanode upon electrochemical oxidation. *Phys. Chem. Chem. Phys.* **2013**, *15* (5), 1443–51.
- (54) Hu, Y.; Boudoire, F.; Hermann-Geppert, I.; Bogdanoff, P.; Tsekouras, G.; Mun, B. S.; Fortunato, G.; Graetzel, M.; Braun, A. Molecular Origin and Electrochemical Influence of Capacitive Surface States on Iron Oxide Photoanodes. *J. Phys. Chem. C* **2016**, *120* (6), 3250–3258.
- (55) Braun, A.; Erat, S.; Zhang, X.; Chen, Q.; Huang, T.-W.; Aksoy, F.; Löhnert, R.; Liu, Z.; Mao, S. S.; Graule, T. Surface and Bulk Oxygen Vacancy Defect States near the Fermi Level in 125 nm $\text{WO}_3\text{-}\delta/\text{TiO}_2(110)$ Films: A Resonant Valence Band Photoemission Spectroscopy Study. *J. Phys. Chem. C* **2011**, *115* (33), 16411–16417.
- (56) Braun, A.; Aksoy Akgul, F.; Chen, Q.; Erat, S.; Huang, T.-W.; Jabeen, N.; Liu, Z.; Mun, B. S.; Mao, S. S.; Zhang, X. Observation of Substrate Orientation-Dependent Oxygen Defect Filling in Thin $\text{WO}_3\text{-}\delta/\text{TiO}_2$ Pulsed Laser-Deposited Films with in Situ XPS at High Oxygen Pressure and Temperature. *Chem. Mater.* **2012**, *24* (17), 3473–3480.
- (57) Bora, D. K.; Hu, Y.; Thiess, S.; Erat, S.; Feng, X.; Mukherjee, S.; Fortunato, G.; Gaillard, N.; Toth, R.; Gajda-Schranz, K.; et al. Between photocatalysis and photosynthesis: Synchrotron spectroscopy methods on molecules and materials for solar hydrogen generation. *J. Electron Spectrosc. Relat. Phenom.* **2013**, *190*, 93–105.
- (58) Tossell, J. A.; Vaughan, D. J.; Johnson, K. H. The Electronic Structure of Rutile, Wustite, and Hematite from Molecular Orbital Calculations. *Am. Mineral.* **1974**, *59* (3–4).
- (59) Braun, A.; Sivula, K.; Bora, D. K.; Zhu, J.; Zhang, L.; Graetzel, M.; Guo, J.; Constable, E. C. Direct Observation of Two Electron Holes in a Hematite Photoanode during Photoelectrochemical Water Splitting. *J. Phys. Chem. C* **2012**, *116* (32), 16870–16875.
- (60) McGuinness, C.; Stagarescu, C. B.; Ryan, P. J.; Downes, J. E.; Fu, D.; Smith, K. E.; Egdell, R. G. Influence of Shallow Core-Level Hybridization on the Electronic Structure of Post-Transition-Metal Oxides Studied using Soft X-Ray Emission and Absorption. *Phys. Rev. B: Condens. Matter Mater. Phys.* **2003**, *68* (16), 165104.
- (61) Bora, D. K.; Braun, A.; Erat, S.; Ariffin, A. K.; Löhnert, R.; Sivula, K.; Töpfer, J. R.; Grätzel, M.; Mancke, R.; Graule, T.; et al. Evolution of an Oxygen Near-Edge X-ray Absorption Fine Structure Transition in the Upper Hubbard Band in $\alpha\text{-Fe}_2\text{O}_3$ upon Electrochemical Oxidation. *J. Phys. Chem. C* **2011**, *115* (13), 5619–5625.
- (62) Wang, S.; Mao, W. L.; Sorini, A. P.; Chen, C.-C.; Devereaux, T. P.; Ding, Y.; Xiao, Y.; Chow, P.; Hiraoka, N.; Ishii, H.; et al. High-pressure evolution of Fe_2O_3 electronic structure revealed by x-ray absorption. *Phys. Rev. B: Condens. Matter Mater. Phys.* **2010**, *82* (14), 144428.

(63) Park, T.-J.; Sambasivan, S.; Fischer, D. A.; Yoon, W.-S.; Misewich, J. A.; Wong, S. S. Electronic Structure and Chemistry of Iron-Based Metal Oxide Nanostructured Materials: A NEXAFS Investigation of BiFeO₃, Bi₂Fe₄O₉, α -Fe₂O₃, γ -Fe₂O₃, and Fe/Fe₃O₄. *J. Phys. Chem. C* **2008**, *112* (28), 10359–10369.

(64) Gregg, B. A. Interfacial Processes in the Dye-Sensitized Solar Cell. *Coord. Chem. Rev.* **2004**, *248* (13–14), 1215–1224.